RSC Advances

ROYAL SOCIETY OF CHEMISTRY

www.rsc.org/advances

Cite this: DOI: 10.1039/c0xx00000x

www.rsc.org/xxxxxx

ARTICLE TYPE

A post-oxidation strategy for the synthesis of graphene/carbon nanotube-supported polyaniline nanocomposites as advanced supercapacitor electrodes

Dechao Lv,[†][a] Jiali Shen,[†][a] Gengchao Wang*[a]

Received (in XXX, XXX) Xth XXXXXXXXX 20XX, Accepted Xth XXXXXXXXX 20XX
DOI: 10.1039/b000000x

A post-oxidation strategy was proposed to synthesize sulfonated graphene nanosheets/carboxylated multi-walled carbon nanotube-supported PANI (*s*GNS/*c*MWCNT@PANI) hierarchical nanocomposites by an interfacial polymerization as advanced supercapacitor electrodes. Field emission scanning electron microscopy (FE-SEM) and high resolution transmission electron microscopy (HRTEM) indicated that the morphology with a coexisting structure of *s*GNS supported PANI nanorod arrays and coaxial *c*MWCNT/PANI nanocables did not show significant difference through a post-oxidation process. X-ray diffraction (XRD) and thermogravimetic analysis (TGA) proved that the oligomers of PANI were eliminated during post-oxidation process. The spectral analysis revealed that the post-oxidation led to the increasing content of quinoid structure in nanocomposites. Electrochemical measurements showed that the *s*GNS/*c*MWCNT@PANI with post-oxidation process exhibited improved cycling stability with 91.4% capacitance retention after 5000 cycles.

1. Introduction

Supercapacitors, bridging secondary batteries and conventional dielectric capacitors, exhibit high specific power, reasonable specific energy and long cycle life.[1-5] These intriguing features have created a great interest towards the application of supercapacitors in the field of memory protection, consumer electronics, energy management, electric vehicles and so on.[6-8] To develop advanced supercapacitors, the active electrode materials with high capacity performance are indispensable.[2, 9-11] Polyaniline (PANI), one of the most promising and versatile conducting polymers, has captured the intense attention for the potential pseudocapacitor application due to its low cost, easy to synthesis, high electrical conductivity and unique pseudo-capacitance properties.[12-14] Unfortunately, the main drawback of PANI is the poor cycling stability, which derived from three aspects: (1) volumetric change such as swelling, shrinking, cracks or breaking due to repeated insertion/de-insertion of ions during the charge/discharge process; (2) the weight loss of active material peeling off from the current collector into the electrolyte; (3) oligomers adhered onto the polyaniline (PANI) during the polymerization process. This restricts its practical application in supercapacitors.[8, 15-17]

Thus, considerable research has been conducted to enhance the cycling stability of PANI. Nanostructured PANI can release the cycling degradation problems caused by volumetric changes or structural conformation[18-20] and enhance active region surface area with electrolyte.[21-23] Ordered and highly aligned nanorods of polyaniline (PANI) were synthesized with 10 nm diameter on transparent ITO substrate using nanotemplate by B.K. Kuila et al, which show good charge/discharge cycle after 1000 cycles.[24] Alternatively, the incorporation of PANI with various nanocarbon materials has been proved to be an effective solution because of the synergetic effects between PANI and nanocarbon. Previous studies demonstrated that binary composites of PANI with ordered mesoporous carbon,[16, 25-28] graphene,[29-34] carbon nano-fibers[18, 35] or carbon nanotubes[29, 36-40] show improvement in the electrochemical stability but with no significant reinforcement for practical applications. For example, a capacity loss comes to 13% after 1000 cycles for PANI/GNS composite ($GP_{6:94}$) via in- situ polymerization of aniline monomer in the presence of graphene suspension and $HClO_4$ solution by J. Li et al.[41] While ternary composites of PANI with 3D interpenetrating network could significantly relieve the cycle degradation problem owing to the unique nanocarbon substrate for accommodating the volu-metric change of PANI.[42-45] Currently, synthesis of nanocarbon supported PANI ternary composites is focusing on obtaining uniform structured PANI on nanocarbon substrate either by electrochemical polymerization[31, 38, 46] or in situ polymerization[43-45, 47]. However, the electrochemical polymerization is not suitable for amplification production due to the low yield of PANI. In situ polymerization is hard to obtain the PANI with high degree of polymerization[48, 49] and ordered structure due to the oligomers randomly deposited on or free from the nanocarbon substrate, which restricts further improvement of the cycling stability for PANI.[50] To the best of our knowledge, no publications with respect to the strategy to eliminate the PANI oligomers of ordered nanocarbon@PANI composites have been reported.

Herein, the hierarchical nanocomposites based on sulfonated graphene nanosheets/carboxylated multi-walled carbon nanotube-supported PANI (*s*GNS/*c*MWCNT@PANI) were synthesized to eliminate the oligomers of PANI by interfacial polymerization with a post-oxidation strategy. The effect of post-oxidation process on the morphology, microstructure and electrochemical performance of as-prepared nanocomposites were discussed in details.

2. Experimental

2.1 Synthesis of *s*GNS/*c*MWCNT@PANI ternary composites without and with post-oxidation strategy treatment

The *s*GNS derived from natural graphite powder (30-50 μm, Sinopharm chemical reagent Co., Ltd.) were prepared according to our previous report.[33] Briefly, graphite oxide (GO) was synthesized from natural graphite powder using the Hummers method.[53] Then GO was dispersed in the deionized water with pH of 9~10 adjusted by ammonia solution to form the GO nanosheets after 40 min sonification. The sodium borohydride was added to the above solution at 80 °C for 1 h under constant stirring. Subsequently, the partially reduced GO was sulfonated with aryl-diazonium salt of sulfanilic acid in an ice bath for 2.5 h. Finally, the resulting solution was treated with hydrazine at 95 °C for 12 h to remove the remaining oxygen functional groups. MWCNTs (diameter <8 nm, Chengdu Organic Chemicals Co. Ltd.) were treated in a mixture of concentrated H_2SO_4 and HNO_3 (3:1 v/v) at 60 °C for 48 h to obtain carboxylated MWCNTs (*c*MWCNT).[51]

The *s*GNS/*c*MWCNT@PANI ternary composites were synthesized by an interfacial polymerization method.[52] The typical procedure was as follows: *s*GNS (21 mg) and *c*MWCNT (9 mg) were added into a mixed 1 M H_2SO_4 solution containing 20 ml of isopropyl alcohol and 80 ml of ethanol, and the mixture was sonicated for 15 min to obtain well-dispersed suspension. Then ammonium persulfate (APS, 0.76 g) was dissolved in the above solution to form water phase. Aniline monomer (0.465 g) was dissolved in 100 ml of dichloromethane to form oil phase. The water and oil phases were then carefully transferred to a 600 ml beaker to react for 24 h at 0 °C. Thereafter removed the oil phase and separated the water phase into duplicate. A part of the water phase was filtered, washed with deionized water and ethanol for several times, and then dried at 60 °C under vacuum to obtain the ternary composite without post-oxidation process (named as *s*GNS/*c*MWCNT@PANI-1). The other part (named as *s*GNS/*c*MWCNT@PANI-2) was continued to add a certain amount of APS (mass ratio of PANI/APS is 1/1) with mechanical agitation at 0 °C for more 6 h, then shared with the same treatment procedure like the *s*GNS/*c*MWCNT@PANI-1 sample. Finally, the ternary composite with post-oxidation process is obtained. The dedoped *s*GNS/*c*MWCNT@PANI nanocomposites are obtained by treating the doped *s*GNS/*c*MWCNT@PANI nanocomposites in 10 wt% ammonium hydroxide for 24 h at room temperature.

2.2 Materials characterization

The morphology of the samples was analyzed by field-emission scanning electron microscopy (FE-SEM, Hitachi S4800) and high resolution transmission electron microscopy (HRTEM, JEOL JEM-2100). Fourier transform infrared (FT-IR) spectra were performed by a Nicolet 5700 spectrometer using KBr sample pellets. The ultraviolet-visible (UV-Vis) spectra were obtained with a Shimadzu UV-3600 PC spectrophotometer, and the suspension of the doped and dedoped *s*GNS/*c*MWCNT@PANI ternary composites with a concentration of 1.5 mg/ml was also adopted. X-ray diffraction (XRD) patterns were performed in a Rigaku D/Max 2550 VB/PC X-ray diffractometer using Cu (Kα) radiation with the 2θ-angle recorded from 3° to 60°. X-ray photoelectron spectroscopy (XPS) analysis was carried on an ESCALAB 250Xi instrument using standard lens mode with a spot size of 300 μm. A monochromatic Al Kα X-ray source (1486.6 eV) was used as the excitation source. The pass energy of each element is 100 eV for general scan and 40 eV for the core level spectra. Surface charging effects were corrected with C 1s peak at 284.6 eV as a reference. The weight loss of the samples were measured using thermogravimetric analyzer (TGA, NET-ZSCH STA 449 C) from room temperature to 800 °C at a heating rate of 10 °C min^{-1} under pure nitrogen atmosphere. The electrical conductivities of the samples were determined by a SX 1934 four-probe instrument using compressed pellets at room temperature.

2.3 Preparation of electrodes and electrochemical testing

The working electrodes were prepared by mixing 85wt% active materials, 10 wt % acetylene black, and 5 wt % polytetrafluoroethylene in a mixed solution of deionized water and ethanol (1/9, by volume) to form a homogeneous slurry. The slurry was rolled and then pressed onto the titanium mesh with 10MPa, followed by drying at 80 °C for 3 h. The mass of the working electrode is about 1 mg. The supercapacitor is composed of two symmetrical working electrodes sandwiched by a modified hydrophilic polypropylene separator and the aqueous electrolyte solution of 1 M H_2SO_4.

Cyclic voltammetry (CV), galvanostatic charge-discharge and electrochemical impedance spectroscopy (EIS) measurements were performed on a CHI 660D electrochemical workstation using a three-electrode mode with as-prepared working electrode, an Ag/AgCl (KCl saturated) reference electrode and a Pt counter electrode. The electrolyte was 1 M H_2SO_4 aqueous solution. The potential range for CV and charge/discharge test was 0~0.8 V with 5 mV s^{-1} scan rate. The EIS measurements were carried out in the frequency range of 10^5-10^{-2} Hz. Cycling stability was performed in two-electrode system on a program testing system (LAND CT 2001A).

The specific capacitance of the electrode materials from CV curves can be calculated according to the following equation:

$$C = \frac{\int_{V_1}^{V_2} IdV}{mvV} \quad (1)$$

Where C (F g^{-1}) is the specific capacitance, I is the current response (A), V_1 and V_2 represent, respectively, the initial and final potentials (V), V is the potential window (V), v is the scan rate (mV s^{-1}) and m is the mass of the active material in the electrodes (g).

The specific capacitance (C) of the active electrode material was also determined from the charge/discharge curves using the equation[51]:

$$C = \frac{I\Delta t}{m\Delta V} \quad (2)$$

Where I is discharge current (A), Δt is the discharging time (s), m is the mass of active electrode material on single side (g), and ΔV is the voltage drop (V) upon discharging (excluding the *IR* drop).

3. Results and discussion

The morphology of ternary composites without and with post-oxidation process is characterized by FE-SEM under different magnification in Fig. 1. The FE-SEM image of *s*GNS/*c*MWCNT@PANI-1 (Fig.1a) shows coexisting structure of *s*GNS supported PANI nanorod arrays and coaxial *c*MWCNT/PANI nanocables. PANI nanorods are vertically aligned on the surface of *s*GNS with average diameter of 10-20 nm. In order to further confirm the morphological structure of *c*MWCNT/PANI nanocables, the HRTEM analysis is employed. Fig. 1c shows that the *c*MWCNT/PANI composites are nanocables with a PANI layer of ca. 4 nm in thickness, which is consistent with the FE-SEM images. The *c*MWCNT sandwiched between *s*GNS greatly restrains the aggregation of *s*GNS. After post-oxidation process, the original hierarchical structure of *s*GNS/*c*MWCNT@PANI-2 is still maintained, but the morphology of PANI arrays become fuzzy and the height decrease (Fig.1b and 1d). This phenomenon may be ascribed to partial degradation of PANI chains and the dissolution of PANI oligomers caused by the oxidation of APS during the post-oxidation process. In XPS nitrogen element calculation (Table 1), the content of PANI in ternary composites decreased from 71.7% of *s*GNS/*c*MWCNT@PANI-1 to 49.3% of *s*GNS/*c*MWCN@PANI-2, which is corresponding to the FE-SEM and HRTEM conclusions.

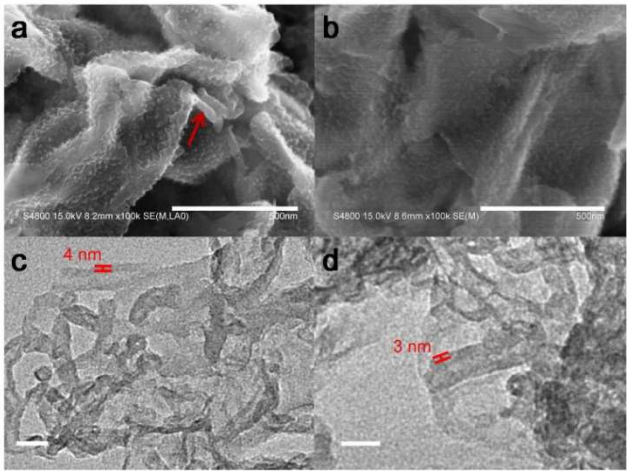

Fig. 1 FE-SEM images of *s*GNS/*c*MWCNT@PANI ternary composites (a) without post-oxidation and (b) with post-oxidation process (scale bars: 500 nm). HRTEM images of *s*GNS/*c*MWCNT@PANI ternary composites (c) without post-oxidation and (d) with post-oxidation process (scale bars: 20 nm).

Fig. 2a shows the FT-IR spectra of doped form *s*GNS /*c*MWCNT@PANI-1 and *s*GNS/*c*MWCNT@PANI-2 ternary composites. Both of the samples exhibit the main infrared-absorption bands which are similar to that of pure PANI. The bands at 1560~1570, 1480~1490, and 1290~1300 cm^{-1} are assigned to the C=C stretching vibration of the quinoid and benzenoid rings as well as the C–N stretching vibration respectively.[42] The relative content of the quinoid and benzenoid rings would be estimated using the relative peak intensity of the quinoid and benzenoid rings.[54] After integral calculation with original data, it is shown that the *s*GNS/*c*MWCNT@PANI-2 composite dispalys a higher ratio (1.3) of the relative peak area of quinoid structure to benzenoid structure, compared with that of 0.56 for *s*GNS/*c*MWCNT@PANI-1. This indicates that *s*GNS/*c*MWCNT@PANI-2 has higher content of quinoid structure in PANI backbone chains, which may be attributed to that the benzenoid structure of ternary composite is converted into the quinoid structure during the post-oxidation process.[41,42,55]

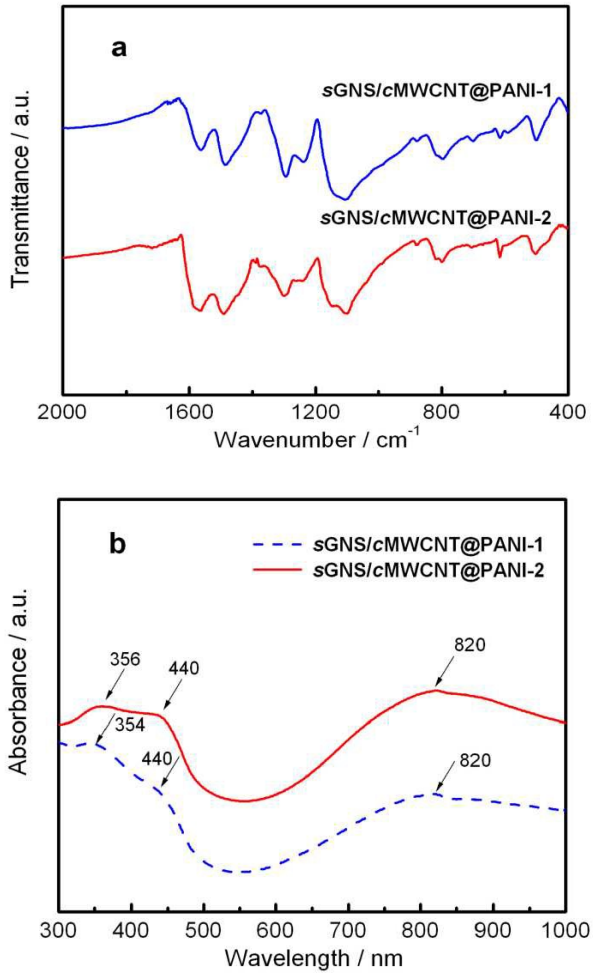

Fig. 2 (a) FT-IR spectra and (b) UV-Vis spectra of doped form *s*GNS/*c*MWCNT@PANI-1 and *s*GNS/*c*MWCNT@PANI-2 nanocomposites.

The chemical structure of PANI in ternary composites could be further characterized by UV−Vis analysis. As shown in Fig. 2b, both of doped form *s*GNS/*c*MWCNT@PANI ternary composites without and with post-oxidation exhibit the same three absorption bands. The bands at around 355 nm can be attributed to π–π^* transition of the benzenoid rings, while the bands at 440 and 820 nm can be assigned to n–π^* transition of the

quinoid rings and polaron transition respectively.[40] Compared with the *s*GNS/ *c*MWCNT@PANI-1, the intensity ratio of the band at 440 nm to that at 355 nm for *s*GNS/*c*MWCNT@PANI-2 has increased. This phenomenon is ascribed to the increasing content of quinoid structure after post-oxidation in ternary composite, which is consistent with the above FT-IR results. The UV−vis spectra of dedoped form *s*GNS/*c*MWCNT@PANI composites further prove this point (Fig. S1).

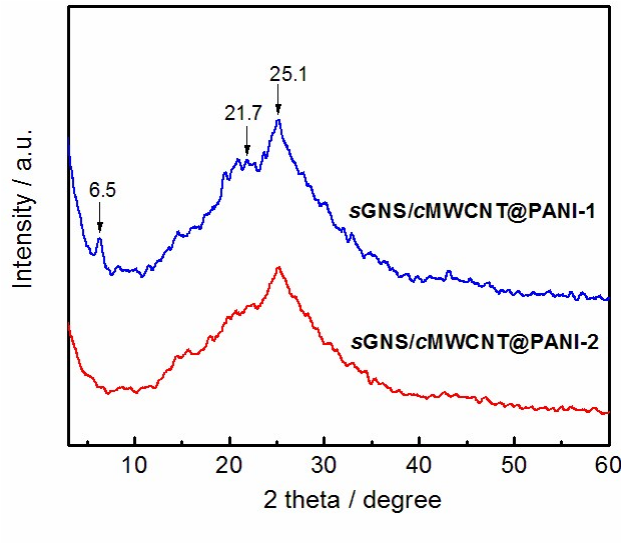

Fig. 3 XRD patterns of *s*GNS/*c*MWCNT@PANI-1 and *s*GNS/*c*MWCNT@PANI-2 nanocomposites.

Fig.3 shows the XRD patterns of *s*GNS/ *c*MWCNT@PANI-1 and *s*GNS/*c*MWCNT@PANI-2 ternary composites. It is clear that both of the composites exhibit two reflection peaks at 2θ = 21.7° and 25.1°, which are corresponding to periodically parallel and vertical to PANI chains respectively.[47] This phenomenon can be attributed to highly ordered PANI nanorod arrays. Besides, the *s*GNS/*c*MWCNT@PANI-1 still shows a weak peak at 2θ = 6.5°, which is corresponding to PANI oligomers. However, when talking about the *s*GNS/*c*MWCNT@PANI-2, a peak at 6.5° disappears and a peak at 21.7° becomes weak. These would suggest that the oligomers and imperfect structure of PANI are eliminated during the post-oxidation process.

The TGA curves of dedoped form *s*GNS/*c*MWCNT@PANI-1 and *s*GNS/*c*MWCNT@PANI-2 are shown in Fig. 4. Both of ternary composites show three main weight losses trend. The first step of weight loss below ca. 290 °C corresponds to the expulsion of absorbed water and small molecular compounds. The second step of weight loss occurs in the range of 290~510 °C due to the decomposition of PANI chains and the removal of sulfonic acid groups in *s*GNS. Then the third weight loss above 510 °C is attributed to the combustion of carbon skeleton of *s*GNS/ *c*MWCNT carrier and further degradation of PANI chains.

It is found that the first and third steps of decomposition behaviour are similar. However, the decomposition behaviors in second step of two samples are clearly different. The weight loss of *s*GNS/*c*MWCNT@PANI-1 (1.8%) in the range of 290~320 °C is larger than that of *s*GNS/*c*MWCNT@PANI-2 (1.1%), which means that the oligomers of PANI in composites are eliminated by post-oxidation process. This result is also supported by the above XRD analysis.

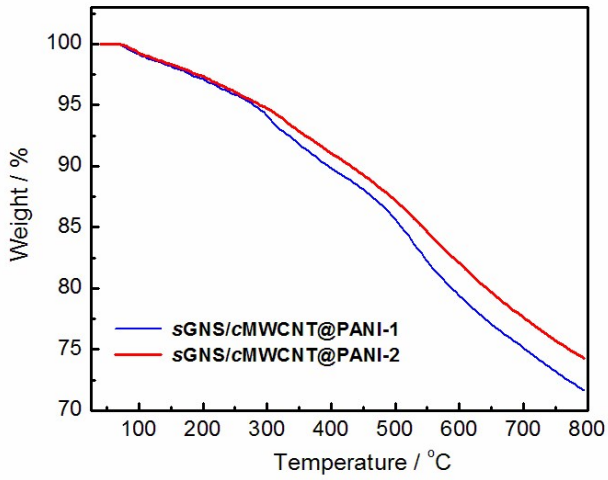

Fig. 4 TGA curves of dedoped form *s*GNS/*c*MWCNT@PANI-1 and *s*GNS/*c*MWCNT@PANI-2 ternary composites.

To determine the chemical composition and structure of *s*GNS/*c*MWCNT@PANI-1 and *s*GNS/*c*MWCNT@PANI-2, the X-ray photoelectron spectroscopy analysis is employed. As shown in Fig. 5a, both of ternary composites display C*1s*, N*1s*, O*1s* and S*2p* peaks, which is indicating the existence of doped form PANI. The N, S and PANI contents for two nanocomposites are calculated from the XPS survey spectra in Table 1. It is apparent that *s*GNS/*c*MWCNT@PANI-2 has less relative amount

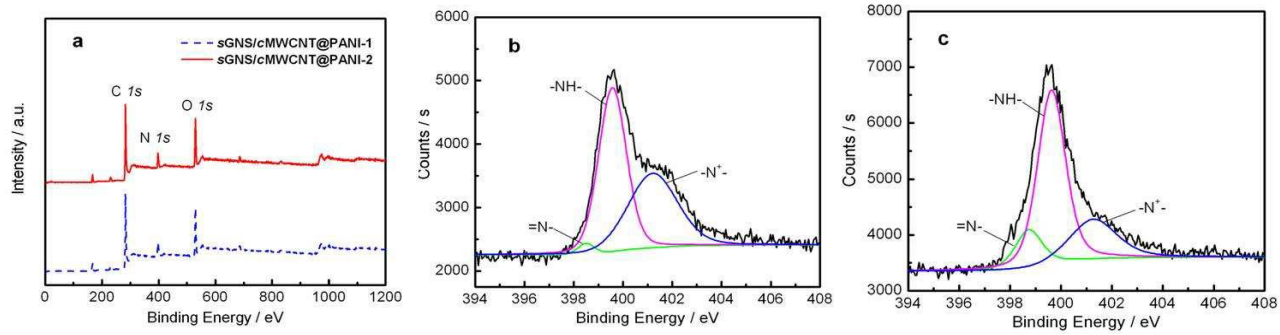

Fig. 5 (a) XPS spectra with survey scan of *s*GNS/*c*MWCNT@PANI-1 and *s*GNS/*c*MWCNT@PANI-2 ternary composites. N *1s* core level XPS spectra for (b) *s*GNS/*c*MWCNT@PANI-1 and (c) *s*GNS/*c*MWCNT@PANI-2

Table 1 The nitrogen element and PANI contents, relative area of C*1s* peaks and the $–N^+–$/ (=N– + –NH–) mole ratio of composites measured by XPS.

Samples	Element content (%)		PANI content (%)	Relative Area (%)			$–N^+–$/(=N– +–NH–) (%)
	N	S		=N– 398.5eV	–NH– 399.6eV	$–N^+–$ 401.2eV	
*s*GNS/*c*MWCNT@PANI-1	9.11	3.65	71.7	2.2	54.3	43.5	77
*s*GNS/*c*MWCNT@PANI-2	6.82	1.29	49.3	14.2	61.9	23.9	31.4

of PANI (49.3%) compared with the *s*GNS/*c*MWCNT@PANI-1 (71.7%). The N1s deconvolution XPS spectra for nanocomposites are analyzed by curve fitting. The N*1s* deconvolution spectra of two nanocomposites exhibit three components of the nitrogen bond at 398.5 eV (quinonoid imine, =N–), 399.6 eV (benzenoid imine, –NH–), and 401.2 eV (nitrogen cationic radical, $–N^+–$) respectively (Fig. 5b and 5c). It is noted that the *s*GNS/*c*MWCNT @PANI-1 exhibits higher [$–N^+–$/(=N– + –NH–)] ratio (77%) than that of *s*GNS/*c*MWCNT@PANI-2 (31.4%) (Table 1), indicating the decrease of doping degree of PANI chains after post-oxidation process. All of these may lead to the decrease of the conductivity of *s*GNS/*c*MWCNT@PANI-2 composite.

To evaluate the influence of post-oxidation process on the electrochemical performance of the supercapacitor cells based on *s*GNS/*c*MWCNT@PANI composites, the voltammetry (CV), galvanostatic charge/discharge and electro-chemical impedance spectroscopy (EIS) are performed. Fig. 6a shows the CV curves of the *s*GNS/*c*MWCNT@PANI ternary composites at a scan rate of 5 mV s^{-1} in a 1 M H_2SO_4 solution with and without post oxidation strategy. Both of nanocomposites present two pairs of redox peaks (C1/A1 and C2/A2), which are corresponding to the leucoemeraldine/emeraldine and emerald-dine/pernigraniline structural conversions. These results indicate good pseudo-capacitance characteristics.[52] It is also found that the cathodic peak (C1) of the ternary composite shift to high potential and the intensity of the peak decrease after the post-oxidation process. This would be explained by that the post-oxidation strategy leads to the increase of oxidation degree in PANI backbone and the decrease of the amounts of PANI, which are supported by FT-IR and XPS results. Furthermore, the specific capacitances of the *s*GNS/*c*MWCNT@PANI-1 and *s*GNS/*c*MWCNT@PANI-2 composites obtained from CV curves are 488 and 397 F g^{-1}, respectively.

Fig.6b depicts the Nyquist plots of *s*GNS/*c*MWCNT@PANI nanocomposites measured at frequencies from100 kHz to 0.01 Hz. It is observed that the Nyquist plots show a straight line at the low frequency region and a semicircle at the high frequency region. The straight line, which is nearly parallel to the imaginary axis, reflects the ideal capacitive behavior due to its fast and reversible redox reaction of PANI nanorods. The semicircle corresponds to the charge-transfer resistance (R_{ct}) at the electrode /electrolyte interface. It is apparent that the *s*GNS/*c*MWCNT @PANI-1 has lower R_{ct} (1.5 Ω) than that of *s*GNS/*c*MWCNT @PANI-2 (3.2 Ω), which is also supported by the decrease of conductivity from 8.5 S/cm for *s*GNS/*c*MWCNT@PANI-1 to 7.3 S/cm for *s*GNS/*c*MWCNT@PANI-2 during the post-oxidation process.

The galvanostatic charge-discharge curves of two ternary composites show symmetrical and mirror-like image, which is indicating the reversible redox reaction (Fig. 6c). The specific capacitance of *s*GNS/*c*MWCNT@PANI-2 calculated from galvanostatic charge/discharge curves is 441 F g^{-1} at a current density of 1 A g^{-1}, which is slightly lower than that of *s*GNS /*c*MWCNT@PANI-1 (495 F g^{-1}). The result could correspond to the values from CV curves. Above phenomenon would be explained as follows: on the one hand, the decrease of PANI content leads to the loss of specific capacitance. On the other hand, the increasing content of quinoid structure would be beneficial for the improvement of specific capacitance. As a result, the specific capacitance of ternary composites slightly reduces after post-oxidation. Moreover, as shown in Fig. 6d, *s*GNS/*c*MWCNT@PANI-2 maintains 74% of the initial capacitance with growing current densities from 0.2 to 10 A g^{-1}, inferior to that of *s*GNS/*c*MWCNT@PANI-1 (83%). By contrast, the pure PANI nanorods lost 67.4% of its capacity in the same condition.[32] The excellent rate performance of *s*GNS/*c*MWCNT @PANI composites is ascribed to the excellent rate capability (85.6% of the initial capacitance with the growing current density from 0.2 to 10 A g^{-1}) of *s*GNS/*c*MWCNT binary composite as a support (Fig. 6d).

The cycling stability of the supercapacitors based on the *s*GNS/*c*MWCNT@PANI ternary composites at a current density of 1 A g^{-1} for 5000 cycles are shown in Fig.7a. The capacitance retention of *s*GNS/*c*MWCNT@PANI-2 still maintains 91.4% of its initial capacity after 5000 cycles, while *s*GNS/*c*MWCNT @PANI-1 only keeps 84.7% of its initial capacity. This indicates that the cycling stability of *s*GNS/*c*MWCNT@PANI has been improved after post-oxidation process. In addition, the CV curves before and after 1000 cycles show no obvious change for the *s*GNS/*c*MWCNT@PANI-2 electrode while exhibit significant difference for the *s*GNS/*c*MWCNT@PANI-1 (Fig. S2). So the above analysis further supports the conclusion of improved cycling stability after post-oxidation.

The improved cycling stability of *s*GNS/*c*MWCNT@PANI-2 sample with post-oxidation strategy could be attributed to two aspects: (1) post-oxidation process eliminates PANI oligomers in *s*GNS/*c*MWCNT@PANI and enhances the π-π inter-action effect between PANI chains and the *s*GNS/*c*MWCNT substrate; (2) the hierarchically three-dimensional network structure of ternary composites are not destroyed during the post-oxidation process, the volume expansion and structure destruction of the electrode also be reduced during the charge-discharge cycling.

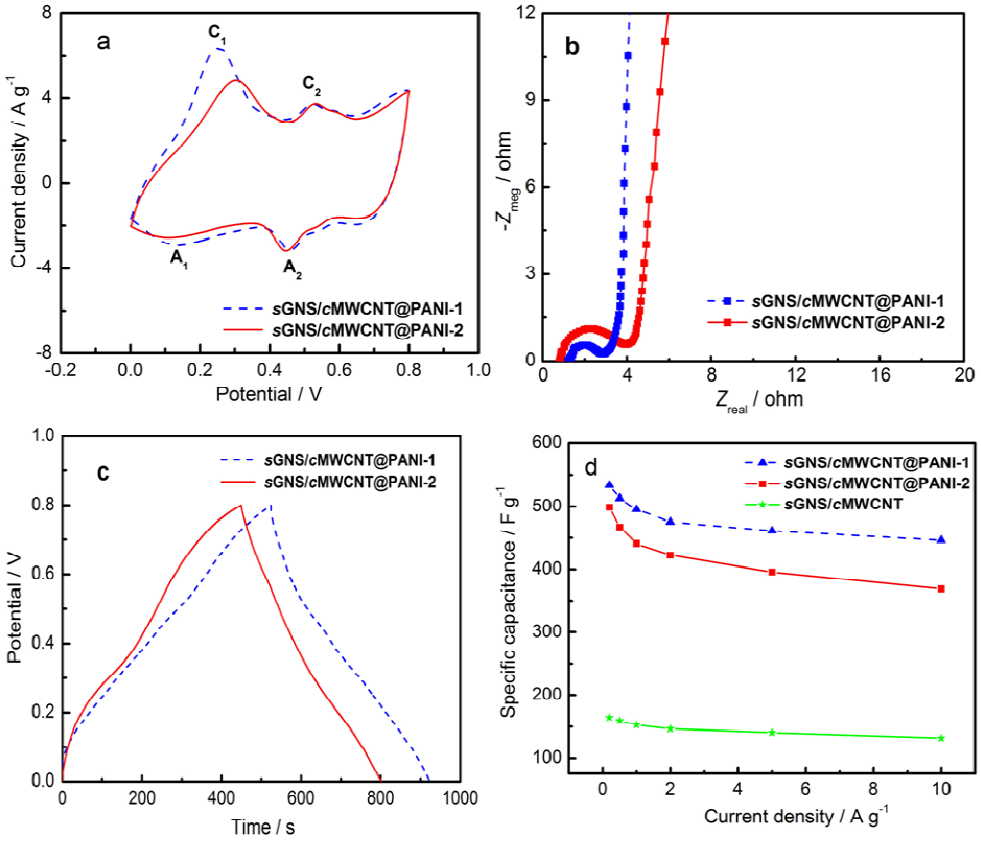

Fig. 6 Electrochemical performance of *s*GNS/*c*MWCNT@PANI ternary composites in 1M H_2SO_4 solution. (a) CV curves at a scan rate of 5 mV s^{-1}. (b) Nyquist plots in the frequency range of 100 kHz to 0.01 Hz. (c) Galvanostatic charge-discharge curves at a current density of 1 A g^{-1}. (d) Specific capacitances of *s*GNS/*c*MWCNT@PANI and *s*GNS/*c*MWCNT composites as a function of various current densities.

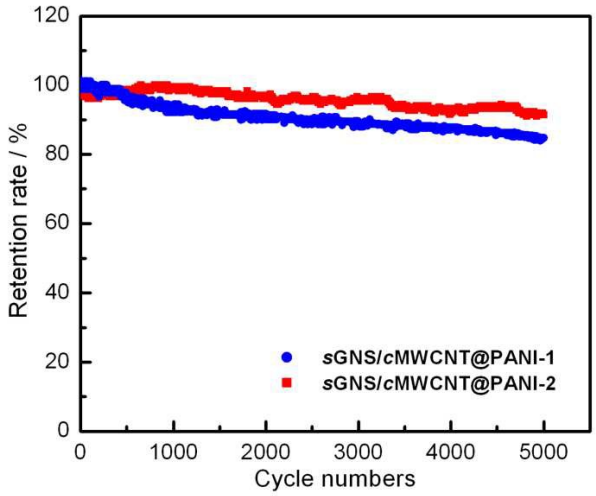

Fig. 7 Cycling stability of the supercapacitors of *s*GNS/*c*MWCNT@PANI-1 and *s*GNS/*c*MWCNT@PANI-2 ternary composites

4. Conclusions

We have reported a post-oxidation strategy to synthesis *s*GNS/*c*MWCNT@PANI ternary nanocomposites as advanced supercapacitor electrodes in this article. After post-oxidation process, the morphology of ternary composites did not show significant difference. The oligomers of PANI were eliminated, as well as the content and doping degree of PANI units was reduced obviously. Besides, the content of quinoid structure of PANI chains has been enhanced. As a result, the specific capacitance and the rate capability of the nanocomposite with post-oxidation process were slightly inferior to that of the sample without post-oxidation treatment. However, *s*GNS/*c*MWCNT@PANI with post-oxidation process exhibits improved cycling stability (91.4% capacitance retention after 5000 cycles) compared to *s*GNS/*c*MWCNT@PANI without post-oxidation (84.7%). The facile post-oxidation strategy can be readily industrialized, providing valuable approach for improving cycling stability of conducting polymers.

Acknowledgements

We greatly appreciate the financial supports of National Natural Science Foundation of China (51173042), Shanghai Municipal Science and Technology Commission (12nm0504102), Fundamental Research Funds for the Central Universities.

Notes and references

†These authors contributed equally to this work.
[a]Shanghai Key Laboratory of Advanced Polymeric Materials, Key Laboratory for Ultrafine Materials of Ministry of Education, School of

Materials Science and Engineering, East China University of Science and Technology, Shanghai 200237, P.R.China.
E-mail: gengchaow@ecust.edu.cn

1 R. J. Brodd, M. Winter, *Chem. Rev.*, 2004, **104**, 4245.
2 P. Simon, Y. Gogotsi, *Nature Materials*, 2008, **7**, 845.
3 C. Liu, F. Li, L. P. Ma and H. M. Cheng, *Adv Mater*, 2010, **22**, 28.
4 S. W. Lee, B. M. Gallant, H. R. Byon, P. T. Hammond and Y.S. Horn ,*Energy & Environmental Science*, 2011, **4**, 1972.
5 F. Beguin, V. Presser, A. Balducci and E. Frackowiak, *Adv Mater*, 2014, **26**, 2283.
6 J. Chen, C. Li and G. Shi, *The Journal of Physical Chemistry Letters*, 2013, **4**, 1244.
7 Y. Huang, J. Liang and Y. Chen, *Small*, 2012, **8**, 1805.
8 K. Wang, H. Wu, Y. Meng and Z. Wei, *Small*, 2014, **10**, 14.
9 Y. Zhu, S. Murali, M. D. Stoller, K. J. Ganesh, W. Cai, P. J. Ferreira, A. Pirkle, R. M. Wallace, K. A. Cychosz, M. Thommes, D. Su, E.A. Stach and R. S. Ruoff, *Science*, 2011, **332**, 1537.
10 J. Yan, Z. Fan, W. Sun, G. Ning, T. Wei, Q. Zhang, R. Zhang, L. Zhi and F. Wei, *Advanced Functional Materials*, 2012, **22**, 2632.
11. G. Yu, X. Xie, L. Pan, Z. Bao and Y. Cui, *Nano Energy*, 2013, **2**, 213
12 H. Cao, X. Zhou, Y. Zhang, L. Chen and Z. Liu, *J. Power Source,*2013, **243**, 715.
13 M. M. Sk, C. Y. Yue and R. K. Jena, *RSC Advances*, 2014, **4**, 5188.
14 H.Xu, J. Zhang, Y. Chen, H. Lu and J. Zhuang, *RSC Advances*, 2014, **4**, 5547.
15 L. Z. Fan, Y. S. Hu, J. Maier, P. Adelhelm, B. Smarsly and M. Antonietti, *Advanced Functional Materials*, 2007, **17**, 3083.
16 L. Li, H. Song, Q. Zhang, J. Yao and X. Chen, *J. Power Sources*,2009, **187**, 268.
17 J. Wei, J. Zhang, Y. Liu, G. Xu, Z. Chen and Q. Xu, *RSC Advances*, 2013, **3**, 3957.
18 Z. P. Zhou, X.F. Wu and H. Q. Hou, *RSC Advances*, 2014, **4**, 23622.
19 H. Zhang, G. Cao, Z. Wang, Y. Yang, Z. Shi and Z. Gu, *Electrochemistry Communications*, 2008, **10**, 1056.
20 H. R. Ghenaatian, M. F. Mousavi, S. H. Kazemi and M. Shamsipur, *Synthetic Metals*, 2009, **159**, 1717.
21 H.M. Zhang, Q. Zhao, S. Zhou, N. Liu, X. Wang, J. Li and F. Wang, *J. Power Sources*, 2011, **196**, 10484.
22 M. M. Sk, C. Y. Yue and R. K. Jena, *Polymer*, 2014, **55**, 798.
23 H. Guan, L.Z. Fan, H. C. Zhang and X. H. Qu, *Electrochimica Acta*, 2010,**56**, 964.
24 B.K. Kuila, B. Nandan, M. Bëhme, A. Janke, M. Stamm, *Chemical Communications*, 2009, 5749-5751.
25 Y. G. Wang, H. Q. Li and Y. Y. Xia, *Advanced Materials*, 2006, **18**, 2619.
26 Y.Q. Dou, Y. Zhai, H. Liu, Y. Xia, B. Tu, D. Zhao and X.X. Liu, *J.Power Sources*, 2011, **196**, 1608.
27 L. Wang, L. Sun, C. Tian, T. Tan, G. Mu, H. Zhang and H. Fu, *RSC Advances*, 2012, **2**, 8359.
28 Y. Yan, Q. Cheng, Z. Zhu, V. Pavlinek, P. Saha and C. Li, *J. Power Sources*, 2013, **240**, 544.
29 J. Li, H. Xie, Y. Li, J. Liu and Z. Li, *J.Power Sources*, 2011, **196**,10775.
30 R. S. Diggikar, D. J. Late and B. B. Kale, *RSC Advances*, 2014, **4**, 22551.
31 P.Manivel, M.Dhakshnamoorthy, A. Balamurugan, N. Ponpandian,D. Mangalaraja and C. Viswanathan,*RSC Advances,2013,***3**,14428.
32 Y. Luo, D. Kong, Y. Jia, J. Luo, Y. Lu, D. Zhang, K. Qiu, C. M. Li and T. Yu, *RSC Advances*, 2013, **3**, 5851.
33 B. Ma, X. Zhou, H. Bao, X. Li and G. C. Wang, *J. Power Source,*2012, **215**, 36.
34 Z. F. Li, H. Zhang, Q. Liu, L. Sun, L. Stanciu and J. Xie, *ACS applied materials & interfaces*, 2013, **5**, 2685.
35 V. Gupta and N. Miura, *J. Power Sources*, 2006, **157**, 616.
36 F. Yang, M. W. Xu, S. J. Bao and Q. Q. Sun, *RSC Advances*, 2014, **4**, 33569.
37 J. Benson, I. Kovalenko, S. Boukhalfa, D. Lashmore, M. Sanghadasa and G. Yushin, *Adv Mater*, 2013, **25**, 6625.
38 Q. Cheng, J. Tang, N. Shinya and L.C. Qin, *J. Power Source,*2013,**241**, 423.
39 X. Lu, H. Dou, S. Yang, L. Hao, L. Zhang, L. Shen, F. Zhang and X. Zhang, *Electrochimica Acta*, 2011, **56**, 9224.
40 M.Q. Sun, G.C. Wang, X. W. Li, Q. L. Cheng and C. Z. Li,*Industrial & Engineering Chemistry Research*, 2012, **51**, 3981.
41 J. Li, H.Q. Xie, Y. Li, J. Liu and Z. X. Li, *J. Power Source,* 2011,**196**, 10775.
42 S.Bhadra, N.K. Singha and D.J. Khastgir, *Appl. Polym. Sci*, 2007, **104**, 1900.
43 R. Ullah, G.A. Bowmaker, C. Laslau, G.I.N. Warerhouse and Z.D. Zujovic, *Synthetic Metals*, 2014, **198**, 203.
44 H. Fan, N. Zhao, H. Wang, J. Xu and F. Pan, *Journal of Materials Chemistry A*, 2014, **2**, 12340.
45 J. Yan, T. Wei, Z. Fan, W. Qian, M. Zhang, X. Shen and F. Wei, *J. Power Sources*, 2010, **195**, 3041.
46 M. Zhong, Y. Song, Y. Li, C. Ma, X. Zhai, J. Shi, Q. Guo and L. Liu, *J. Power Sources*, 2012, **217**, 6.
47 T. Wu, X. Xu, L. Zhang, H. Chen, J. Gao and Y. Liu, *RSC Advances*, 2014, **4**, 7673.
48 S. L. Mu and Y. F. Yang, *Journal of Physical Chemistry*, 2008, **112**, 11558.
49 O. L. Gribkova, A. A. Nekrasov, V. F. Ivanov, V. I. Zolotorevsky and A. V. Vannikov, *Electrochimica Acta*, 2014, **122**, 150.
50 X. Xie, L. Gao, J. Sun, Y. Liu, H. Kajiura, Y. Li and K. Noda, *Carbon*, 2008, **46**, 1145.
51 C. Y. Yang, J. L. Shen, C. Y. Wang, H. J. Fei, H. Bao and G. C. Wang, *Journal of Materials Chemistry A*, 2014, **2**, 1458.
52 J. L. Shen, C. Y. Yang, X. W. Li and G. C. Wang, *ACS applied materials & interfaces*, 2013, **5**, 8467.
53 W.S. Hummers, R.E. Offeman, *J.Am.Chem.Soc,* 1958, **80**,1339.
54 Y.J. Yu, B. Che, Z.H. Si, L. Li, W. Chen and G. Xue, *Synthetic Metals*, 2005, **150**, 271.
55 Q. Huang, G. Chen and J. Liu, *Polym. Adv. Technol*, 2014, **25**, 1391.